NUREG/CR-0264
LA-7404

Fluid-Structure Response of a Pressurized Water Reactor Core Barrel During Blowdown

University of California

LOS ALAMOS SCIENTIFIC LABORATORY
Post Office Box 1663 Los Alamos, New Mexico 87545

NUREG/CR-0264
LA-7404
R4

Fluid-Structure Response of a Pressurized Water Reactor Core Barrel During Blowdown

W. C. Rivard
M. D. Torrey

Manuscript submitted: July 1978
Date published: September 1978

Prepared for
Division of Reactor Safety Research
Office of Nuclear Regulatory Research
US Nuclear Regulatory Commission
Washington, DC 20555

UNITED STATES
DEPARTMENT OF ENERGY
CONTRACT W-7405-ENG. 36

An Affirmative Action/Equal Opportunity Employer

FLUID-STRUCTURE RESPONSE OF A PRESSURIZED WATER REACTOR CORE BARREL DURING BLOWDOWN

by

W. C. Rivard and M. D. Torrey

ABSTRACT

Three-dimensional, coupled, fluid-structure calculations were performed for the dynamics of the core support barrel in an HDR reactor vessel during blowdown. For these calculations we coupled the three-dimensional, two-fluid code K-FIX to the three-dimensional elastic shell code FLX. The results demonstrate the importance of the coupled interaction. We investigated the utility of a two-dimensional fluid description and obtained reasonably good results for displacements and stresses. The influence of a massive ring attached to the core barrel bottom is shown to be predominantly local. Maximum deflection of the core barrel bottom is reduced by the ring because its stiffness is sufficient to preclude any cross-sectional distortion. Without the ring, the total deflection of the core barrel bottom is shown to be more from distortion than displacement of the mass center. A nodalization study indicates the degree of circumferential and axial resolution required for accurate results. Fine axial resolution is needed near the top, built-in boundary of the core barrel to determine stresses accurately, but it is less necessary for displacements.

I. INTRODUCTION

Fluid-structure interaction phenomena affect the dynamics and loads experienced by light water reactor vessel internal structures during a sudden depressurization. To investigate the relative importance of the coupled interaction, we performed three-dimensional calculations for the dynamics of the fluid and core support barrel in an HDR reactor vessel during blowdown. The HDR is a full-scale, previously operational, single loop reactor vessel of German design.[1] Cooperative experimental and analytical studies are being made by the United States and Germany on this vessel.[2,3] The calculational results presented in this report were obtained using initial and boundary data that we felt were typical of these experiments. The results should not be considered as pretest predictions of the experiments; they are presented only to display relative effects. Besides displaying the importance of fluid-structure coupling, our objectives are to investigate (1) the utility of a two-dimensional fluid dynamic simulation in place of the full three-dimensional treatment, (2) the effect of attaching a stiff and massive ring to the core barrel bottom, and (3) the sensitivity of the results to structural noding.

Three-dimensional fluid dynamics is calculated with the K-FIX(3D) code,[4] which solves the two-fluid, six-equation model for two-phase flow. However, for this application, the fluid is entirely subcooled water. The broken cold input leg of the single loop is modeled through a time-dependent pressure boundary condition for present purposes. The core barrel dynamics is described by the linear elastic cylindrical shell equations. These equations are solved by an explicit finite difference algorithm in the FLX code.[5] In Sec. II we list the governing equations for the fluid and shell and describe their coupled solution procedure.

II. FLUID AND SHELL EQUATIONS

The fluid equations solved by K-FIX(3D) reduce to the following set for single-phase liquid flow at constant temperature.

$$\frac{\partial \rho_\ell}{\partial t} + \underline{\nabla} \cdot \rho_\ell \, \underline{u}_\ell = 0 \quad ,$$

$$\frac{\partial \rho_\ell \, \underline{u}_\ell}{\partial t} + \underline{\nabla} \cdot (\rho_\ell \, \underline{u}_\ell \, \underline{u}_\ell) = - \underline{\nabla} p \quad ,$$

and

$$p = p_o + c_\ell^{\,2} \, (\rho_\ell - \rho_{o\ell}) \quad ,$$

where ℓ refers to the liquid phase; ρ, $\underline{u}$, p, and c are density, velocity, pressure, and constant adiabatic sound speed, respectively; and p_o and $\rho_{o\ell}$ are constants. The K-FIX finite difference solution method, described in detail in Ref. 4, reduces to the ICE[6] technique for single-phase liquid flow where the pressure gradient and mass flux are computed with advanced time quantities and the momentum flux is evaluated explicitly. In a computational cell, density and pressure are located at the cell center and the velocity components are centered on the cell faces that are normal to the component's direction. Fluxes are computed with full upstream differencing.

The linear elastic cylindrical shell (structure) equations solved by FLX are the standard Timoshenko equations.[7]

$$\rho h \ddot{U} = N_x' + N_{\phi x}^0 \quad ,$$

$$\rho h \ddot{V} = N_\phi^0 + N_{\phi x}' - M_\phi^0/a + M_{x\phi}'/a \quad ,$$

$$\rho h \ddot{W} = q + M_x'' - 2M_{x\phi}^{0\,\prime} + M_\phi^{0\,0} + N_\phi/a \quad ,$$

where

$$N_x = C(U' + \nu V^0 - \nu W/a) \quad ,$$

$$N_\phi = C(V^0 - W/a + \nu U') \quad ,$$

$$N_{\phi x} = C(1 - \nu)(U^0 + V')/2 \quad ,$$

$$M_x = - D(W'' + \nu W^{00} + \nu V^0/a) \quad ,$$

$$M_\phi = - D(W^{00} + \nu W'' + V^0/a) \quad ,$$

$$M_{x\phi} = D(1 - \nu)(W^{0'} + V'/a) \quad ,$$

and

$$C = Eh/(1 - \nu^2) \quad , \quad D = Eh^3/12(1 - \nu^2) \quad .$$

In these equations U, V, and W are the axial, circumferential, and radial displacements, respectively; ρ is the density; h is the thickness; a is the midplane radius; ν is Poisson's ratio; q is the net pressure differential; and E is Young's Modulus. The superscript prime denotes differentiation with respect to the axial coordinate x, and the superscript zero denotes differentiation with respect to the circumferential coordinate $a\phi$. For the Timoshenko equations, the radial displacements are positive inward. Velocities and displacements are computed from the accelerations as

$$\dot{U}^{n+1} = \dot{U}^n + \delta t_s \ddot{U}^{n+1} \quad ,$$

$$\dot{V}^{n+1} = \dot{V}^n + \delta t_s \ddot{V}^{n+1} \quad ,$$

$$\dot{W}^{n+1} = \dot{W}^n + \delta t_s \ddot{W}^{n+1} \quad ,$$

and

$$U^{n+1} = U^n + \delta t_s \dot{U}^{n+1} \quad ,$$

$$V^{n+1} = V^n + \delta t_s \dot{V}^{n+1} \quad ,$$

$$W^{n+1} = W^n + \delta t_s \dot{W}^{n+1} \quad ,$$

where $\dot{U}$, $\dot{V}$, and $\dot{W}$ are the velocity components, $\ddot{U}$, $\ddot{V}$, and $\ddot{W}$ are the accelerations, and δt_s is the structure time step. Displacements, velocities, accelerations, and the pressure differential are located at the center of a structure finite difference cell. In the FLX code, cells have the same circumferential length but may have different axial lengths. The boundary conditions at the top, built-in boundary of the core barrel are

$$U(\phi,0) = V(\phi,0) = W(\phi,0) = W'(\phi,0) = 0 \quad ,$$

and at the bottom, free boundary are

$$M_x(\phi,L) = M_{x\phi}(\phi,L) = N_x(\phi,L) = N_{\phi x}(\phi,L) = 0 \quad .$$

The solution of the fluid and structure equations is coupled through the fluid pressure field that enters the structure equations as the net pressure differential q and the structure velocity that enters the fluid equations as a moving boundary. The structure equations generally are integrated several time steps δt_s for each fluid time step δt. The diffusional limitations on the structure time step for explicit integrations are

$$\delta t_s \leq 2\delta x \left\{\rho(1 - \nu^2)/E\left[2 + (1 - \nu)\,(\delta x/a\delta\phi)^2\right]\right\}^{1/2}$$

from the axial acceleration equation,

$$\delta t_s \leq 2\delta x \left\{\rho(1 - \nu^2)/E\left[1 - \nu + 2\,(\delta x/a\delta\phi)^2\right]\right\}^{1/2}$$

from the circumferential acceleration equation, and

$$\delta t_s \leq 0.5\,(a\delta\phi)^2\,\delta x^2\left[6(1 - \nu^2)\rho/E\right]^{1/2}/h\left[(a\delta\phi)^2 + \delta x^2\right]$$

from the radial acceleration equation for $(h/a)^2 \ll 1$.

The results presented in Sec. III were obtained with δt_s 5 to 40 times smaller than δt. These factors are about four times more conservative than would result for δt_s specified by the above inequalities. This ensures that the results obtained for the structure noding study do not reflect any significant time step sensitivity. The pressure differential q at nodal point (m,n) on the structure mesh is calculated from the fluid dynamic pressure field. Pressure differences across the core barrel are computed at the axial and circumferential locations of the fluid cell centers. Linear interpolation between values at these locations is used to obtain values at the locations of the structure nodal points. The reverse of this interpolation is used to transfer the negative radial velocity components of the structure to the radial velocity component array for the fluid. The change in algebraic sign is required because the structure equations have the radial direction positive inward rather than outward as it is in the fluid equations. The motion of the core barrel causes a fractional change in volume δVOL/VOL for the fluid cells adjacent to the core barrel and a corresponding density change

$$\delta\rho_\ell = -\rho_\ell\,\delta\mathrm{VOL}/\mathrm{VOL} \quad .$$

With a single cell across the downcomer gap, the density in the downcomer cells changes according to

$$(\delta\rho_\ell)_{I,j,k} = -\delta t\left[<\rho_\ell v_\ell>_{I,j,k}/\delta z + <\rho_\ell w_\ell>_{I,j,k}/(r_I\,\delta\theta)\right]$$

$$+\delta t\,(\rho_\ell)_{I,j,k}\,(u_\ell)_{I-\frac{1}{2},j,k}\,r_{I-\frac{1}{2}}/(r_I\,\delta r)\ ,$$

where I is the radial index of cells in the downcomer gap; j and k are their axial (z) and circumferential (θ) indices, respectively; and $<\rho_\ell v_\ell>$ and $<\rho_\ell w_\ell>$ are the mass fluxes in the axial and circumferential directions, respectively. The last term accounts for the effect of volume change where $r_{I-1/2}$ and r_I are the radial coordinates of the cell's inner boundary, which coincides with the outer boundary of the core barrel, and the cell's center. The last term has the form of a radial flux term for donor cell differencing, except that the density used does not depend on the algebraic sign of $(u_\ell)_{I-1/2,j,k}$. The flux on the cell's outer boundary is zero because the vessel is considered rigid. A similar expression describes the density change for cells (I−1,j,k) in the core region adjacent to the core barrel. For these cells

$$(\delta\rho_\ell)_{I-1,j,k} = -\delta t\left[<\rho_\ell v_\ell>_{I-1,j,k}/\delta z + <\rho_\ell w_\ell>_{I-1,j,k}/(r_{I-1}\,\delta\theta)\right]$$

$$-\delta t\left\{(\rho_\ell)_{I-1,j,k}\,(u_\ell)_{I-\frac{1}{2},j,k}\,r_{I-\frac{1}{2}} - (u_\ell)_{I-3/2,j,k}\,r_{I-3/2}\right.$$

$$\left.\left[(\rho_\ell)_{I-1,j,k}\ \text{or}\ (\rho_\ell)_{I-2,j,k}\right]\right\}/r_{I-1}\,\delta r\ ,$$

where $(\rho_\ell)_{I-1,j,k}$ is used for the radial flux if $(u_\ell)_{I-3/2,j,k}$ is negative and $(\rho_\ell)_{I-2,j,k}$ is used if $(u_\ell)_{I-3/2,j,k}$ is positive. The flux on the outer boundary of this cell uses $(\rho_\ell)_{I-1,j,k}$ to account for the effect of volume change regardless of the algebraic sign of $(u_\ell)_{I-1/2,j,k}$.

The radial velocity component on the outer boundary of cell (I−1,j,k) is not calculated as part of the fluid solution because it is determined by solution of the structure equations. The core barrel velocities remain fixed during the iterative solution of the fluid mass and momentum equations. Because there is no radial flow across the core barrel, certain momentum flux terms must vanish. These are the fluxes of axial and circumferential momentum by radial velocity across the inner boundary of the cell (I,j,k), the same fluxes across the outer boundary of cell (I−1,j,k), and the radial flux of radial momentum across the center of this cell when $(u_\ell)_{I-1,j,k} + (u_\ell)_{I-2,j,k}$ is negative.

This coupling technique has been used successfully with one-, two-, and three-dimensional fluid dynamic simulations. The results with one-dimensional fluid dynamics that exhibit axial, circumferential, and radial motion separately have been compared with analytic solutions for structure frequency, displacement, and added mass effects.[5,8]

III. COMPUTATIONAL RESULTS

A. Coupling Sensitivity

The results presented here were obtained for the HDR pressurized water reactor vessel shown in Fig. 1. The broken cold leg of the single loop is represented by a single computational cell that

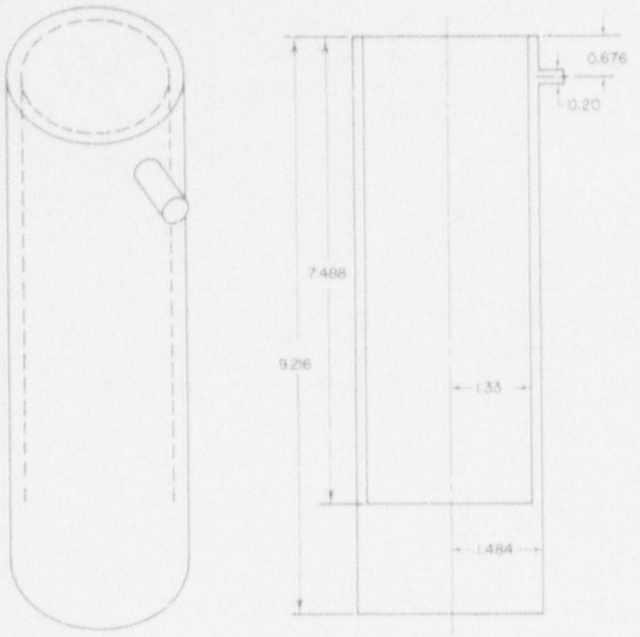

Fig. 1.
Geometry of HDR pressurized water reactor vessel. Dimensions are in meters.

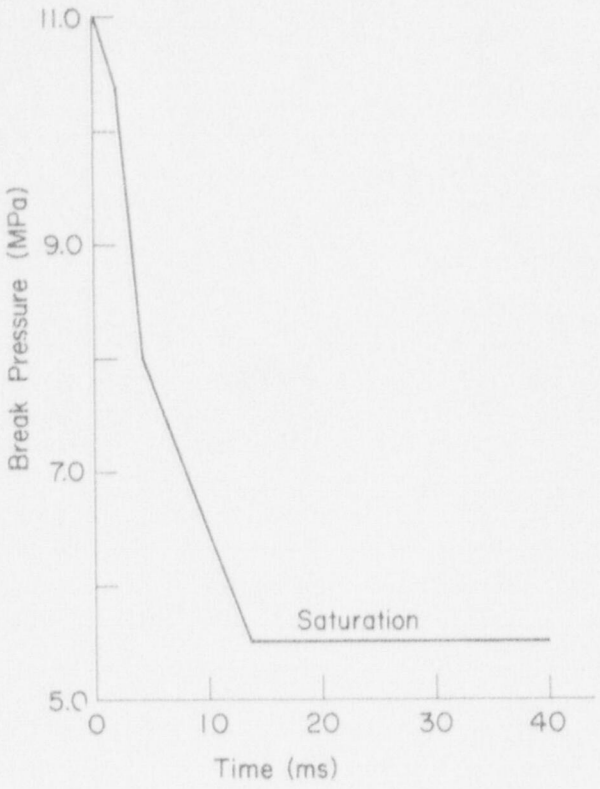

Fig. 2.
Prescribed pressure history at the cold leg break that is used as a boundary condition for the calculations.

extends 15 cm beyond the reactor vessel. A time varying pressure, as shown in Fig. 2, is specified in this cell to simulate the break. Because of symmetry, 180° of the vessel is calculated. The plane $\theta = 0°$ contains the centerline of the broken pipe. The vessel is filled with water at 543 K and pressurized to 11.0 MPa. The constants that enter the fluid and structure equations have values $p_o = 11.0$ MPa, $\rho_{o\ell} = 732.8$ kg/m^3, $c_\ell = 992.7$ m/s, $E = 1.7 \times 10^5$ MPa, $h = 0.023$ m, $a = 1.318$ m, $\nu = 0.3$, and $\rho = 7800$ kg/m^3. The fluid regions are zoned so that $\delta r = 0.4433$ m in the core and lower plenum, $\delta r = 0.154$ m in the downcomer gap, and δz and $\delta\theta = 0.288$ m and 0.2094 rad (12°), respectively, in all regions. The total number of fluid cells is 3468, which includes the perimeter cells used to specify boundary conditions. The fluid time step of $\delta t = 50$ μs is small enough to ensure that pressure waves are followed accurately. For solution of the shell equations, noding of the core barrel is the same for all cases except those that specifically investigate spatial resolution effects. At the end of this section we discuss these latter cases and describe their various nodings. The standard structural noding has 448 nodes and uses 12° intervals circumferentially ($a\delta\phi = 0.2760$ m) with $\phi = 0°$ coinciding with $\theta = 0°$ and a nonuniform axial distribution. The first axial level is located at the top, built-in boundary where $x = 0$, and the second level is at $x = 0.144$ m. Levels 3 through 27 are equally spaced ($\delta x = 0.288$ m) beginning at $x = 0.432$ m and ending at $x = 7.344$ m. The last level is at the bottom, free boundary of the core barrel where $x = 7.488$ m. This axial spacing is particularly convenient for coupling with the fluid equations, because the nodes coincide with the axial positions of the fluid cell centers where pressures are located and with the centers of the cell faces where the radial velocity components are located. The time step for integrating the structure equations is $\delta t_s = 10$ μs, which is four

times more conservative than the diffusional limitations cited earlier. For this calculation, these limitations are $\delta t_s \leq 40\ \mu s$, $\delta t_s \leq 53\ \mu s$, and $\delta t_s \leq 177\ \mu s$ from the axial, circumferential, and radial acceleration equations, respectively.

Figures 3a-d show the relative importance of fluid-structure coupling. Note that in these and the following figures that show radial deflections of the core barrel, outward deflections are plotted as positive, which is contrary to the sign convention of the Timoshenko equations. Radial flections of the core barrel in the $\phi = 0°$ plane are shown at 10, 20, 30, and 40 ms after the pipe break. The uncoupled results are calculated by integrating the structure equations subject to the fluid dynamic pressure field but not returning the structure velocity back for integration of the fluid equations. In this way the resulting fluid dynamic solution is the same as for a rigid core barrel. The deflection profiles at 10 ms indicate a substantial attenuation of the pressure release wave speed for the coupled case. A similar attenuation in wave speed is well known for wave propagation through a fluid contained in a tube with distensible walls. The inward deflection of the lower portion of the core barrel seen at 10 and 20 ms is induced to accommodate fluid displaced downward from the upper region of the downcomer gap by the outward deflection in that region. Motions of the core barrel bottom directly below the break are compared in Fig. 4. The frequency and amplitude are reduced substantially for the coupled case. The axial bending stresses at the core barrel top are compared in Figs. 5a-d. This axial bending stress is shown later to be the most significant stress at this location, which is often the location of maximum stress. The axial bending stress is calculated from the axial bending moment per unit of circumferential length through the relation

$$M_x = \int_{-h/2}^{h/2} \eta\, \sigma_x(\eta; x, \phi)\, d\eta \quad .$$

Integration of this expression yields

$$\sigma_{zb} = 6\, M_x/h^2 \quad ,$$

when the antisymmetric part of $\sigma_x(\eta;x,\phi)$ is approximated as

$$\sigma_x(\eta; x, \phi) \approx 2\eta\, \sigma_{zb}/h \quad .$$

The significant influence of the coupling on the stress is apparent in Fig. 5, as well as in Fig. 6, which shows the time histories of the stress at the core barrel top in the plane $\phi = 0°$. The coupled calculation takes 56 min of CDC 7600 time, whereas the uncoupled calculation takes 52 min. Calculation of the three-dimensional fluid dynamics alone requires 50 min.

B. Two- and Three-Dimensional Comparisons

Because fluid velocities in the lower plenum and core are small relative to those in the downcomer gap, we investigated the utility of two-dimensional fluid calculations for describing the core barrel dynamics and stress. For two-dimensional calculations to be successful to 40 ms after the break, the resulting depressurization in the lower plenum and core must be modeled. Within 40 ms the pressure in these regions drops to about 9.5 MPa, which is about 1.5 MPa less

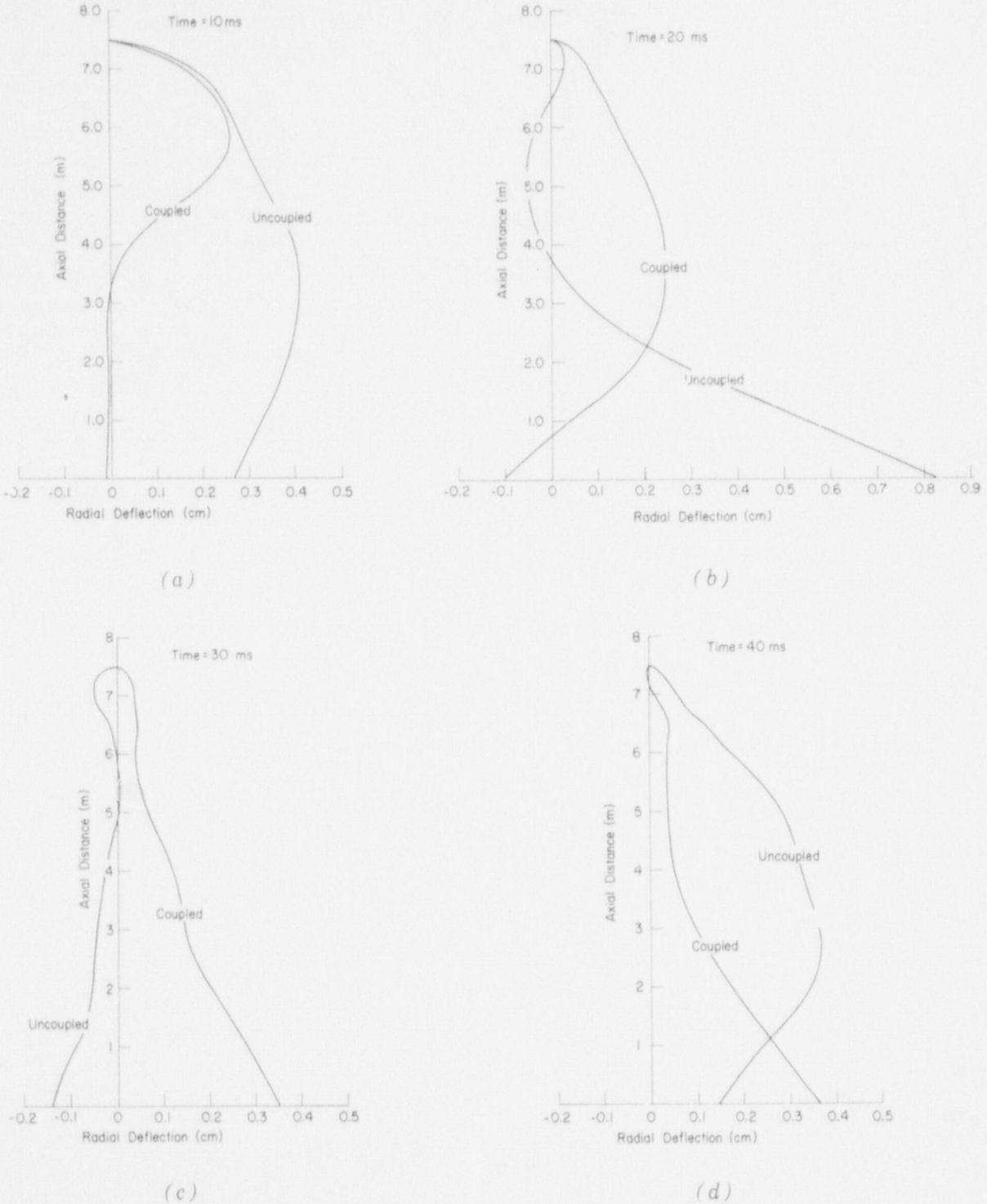

Fig. 3.
Radial deflections of the core barrel in the plane $\phi = 0°$ through the break at 10, 20, 30, and 40 ms after the pipe break. The results were calculated in three dimensions with and without fluid-structure coupling.

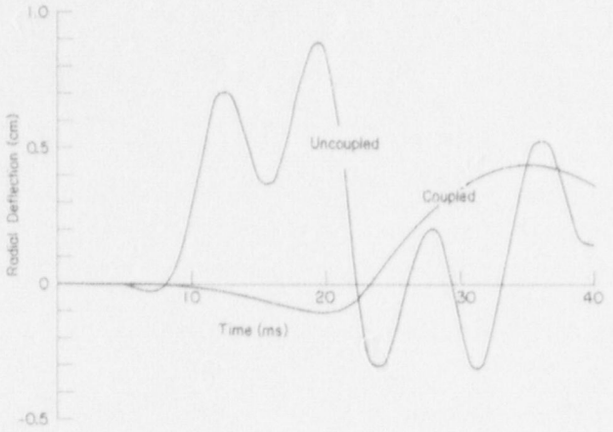

Fig. 4.
Radial deflections of the core barrel bottom directly below the break calculated in three dimensions with and without fluid-structure coupling.

than its initial value. A simple depressurization model was used to calculate the average pressure $\bar{p}$ in the lower plenum and core from the mass efflux through the break; that is,

$$\bar{p} = p_o - c_\ell^2 \text{ (mass loss)/(fluid volume)} .$$

Figure 7 shows a comparison of the average pressure $\bar{p}$ with selected fluid cell pressures from a three-dimensional coupled calculation. The fluid cell pressures P_c and $P_{\ell p}$ are associated with cells at the top of the core 180° around from the break and at the top of the lower plenum directly below the break, respectively. The difference between these two values provides a measure of the pressure gradients in the lower plenum and core. Although small pressure gradients do exist, the curve for $\bar{p}$ provides good average values. The two-dimensional fluid calculation uses the pressure $\bar{p}$ to specify the pressure boundary condition at the bottom of the downcomer. Fluid dynamics is calculated only in the downcomer gap. The pressure $\bar{p}$ also is used for calculating the pressure differential q across the core barrel, which is used in the structural equations. Each fluid time step the value of $\bar{p}$ is updated based on the increment of mass efflux.

The results of two- and three-dimensional calculations are compared in Figs. 8a-d, which show the radial deflection curves through the $\phi = 0°$ plane at 10, 20, 30, and 40 ms. The curves labeled 3D(16,28) are identical to the coupled results shown in Sec. III.A. Quantities in parentheses refer to the circumferential and axial noding of the structure, respectively. The two-dimensional fluid calculation uses the same axial and circumferential cell dimensions as the three-dimensional fluid calculation. The two-dimensional calculation is performed with the three-dimensional K-FIX code by prescribing that the cells in the lower plenum and core be obstacle cells. A total of 476 fluid cells, including the boundary condition perimeter cells, remain in the 180° of the downcomer annulus. Overall agreement between the deflection profiles is satisfactory for this application.

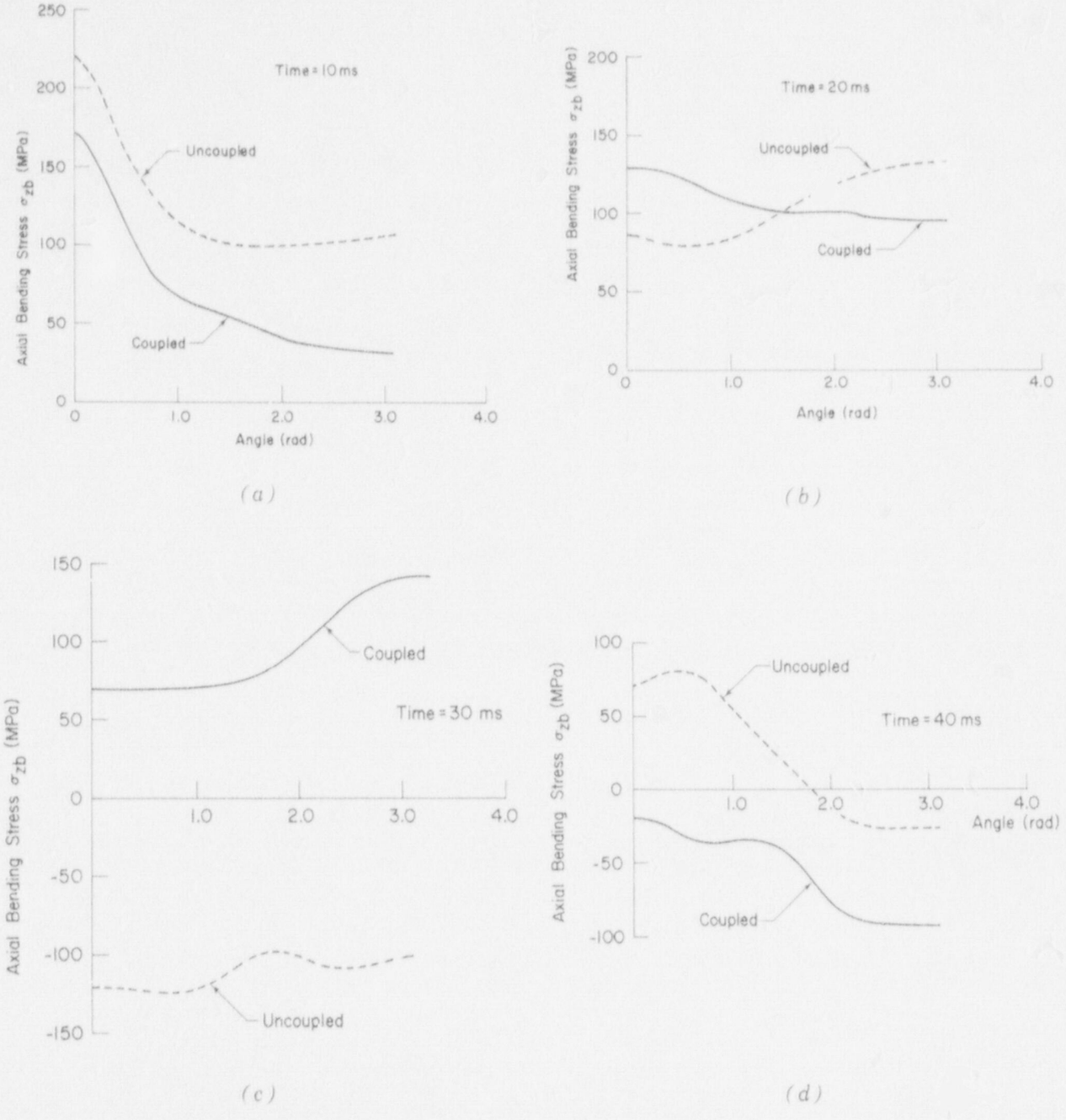

Fig. 5.
Axial bending stresses at the top, built-in boundary of the core barrel calculated in three dimensions with and without fluid-structure coupling at 10, 20, 30, and 40 ms after the pipe break.

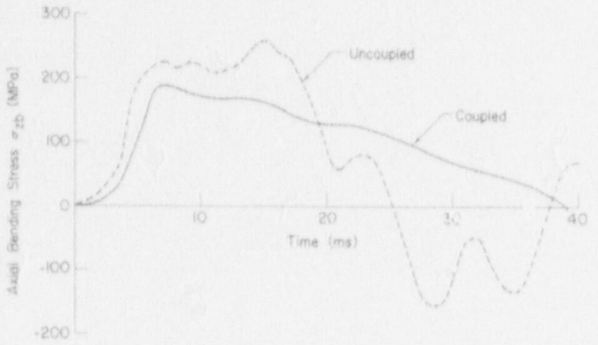

Fig. 6.
Axial bending stresses at the top of the core barrel in the plane $\phi = 0°$ through the break calculated in three dimensions with and without fluid-structure coupling.

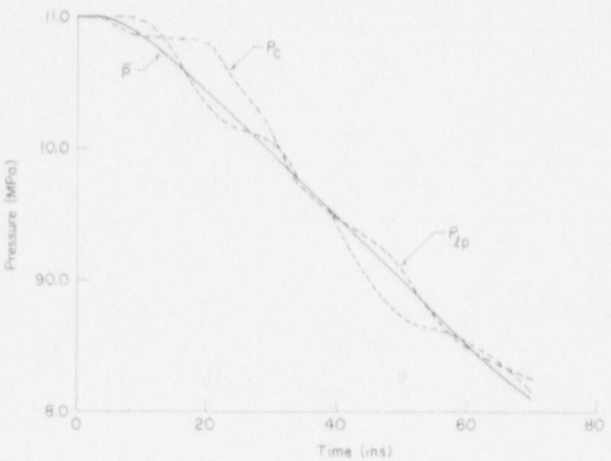

Fig. 7.
Comparison of typical lower plenum and core pressures, P_{lp} and P_c, with the average pressure $\bar{p}$ computed from the mass efflux. The curves were obtained from a three-dimensional coupled calculation.

Figures 9a-d show the calculated stresses at the core barrel top from the three-dimensional, coupled calculation. The bending stress $\sigma_{\theta b}$ is calculated from the circumferential bending moment per unit of axial length M_ϕ, which is similar to the calculation of σ_{zb} from M_x. The axial normal stress σ_{zn} is calculated from the axial normal force per unit of circumferential length through the relation

$$N_x = \int_{-h/2}^{h/2} \sigma_x(\eta; x, \phi)\, d\eta \quad .$$

Integration yields

$$\sigma_{zn} = N_x/h$$

when the symmetric part of $\sigma_x(\eta;x,\phi)$ is approximated as a constant σ_{zn}. The normal stress $\sigma_{\theta n}$ is obtained similarly from N_ϕ. The shearing stress τ_s is obtained through the relation

$$N_{\phi x} = \int_{-h/2}^{h/2} \tau_{\phi x}(\eta; x, \phi)\, d\eta \quad .$$

Integration yields

$$\tau_s = N_{\phi x}/h$$

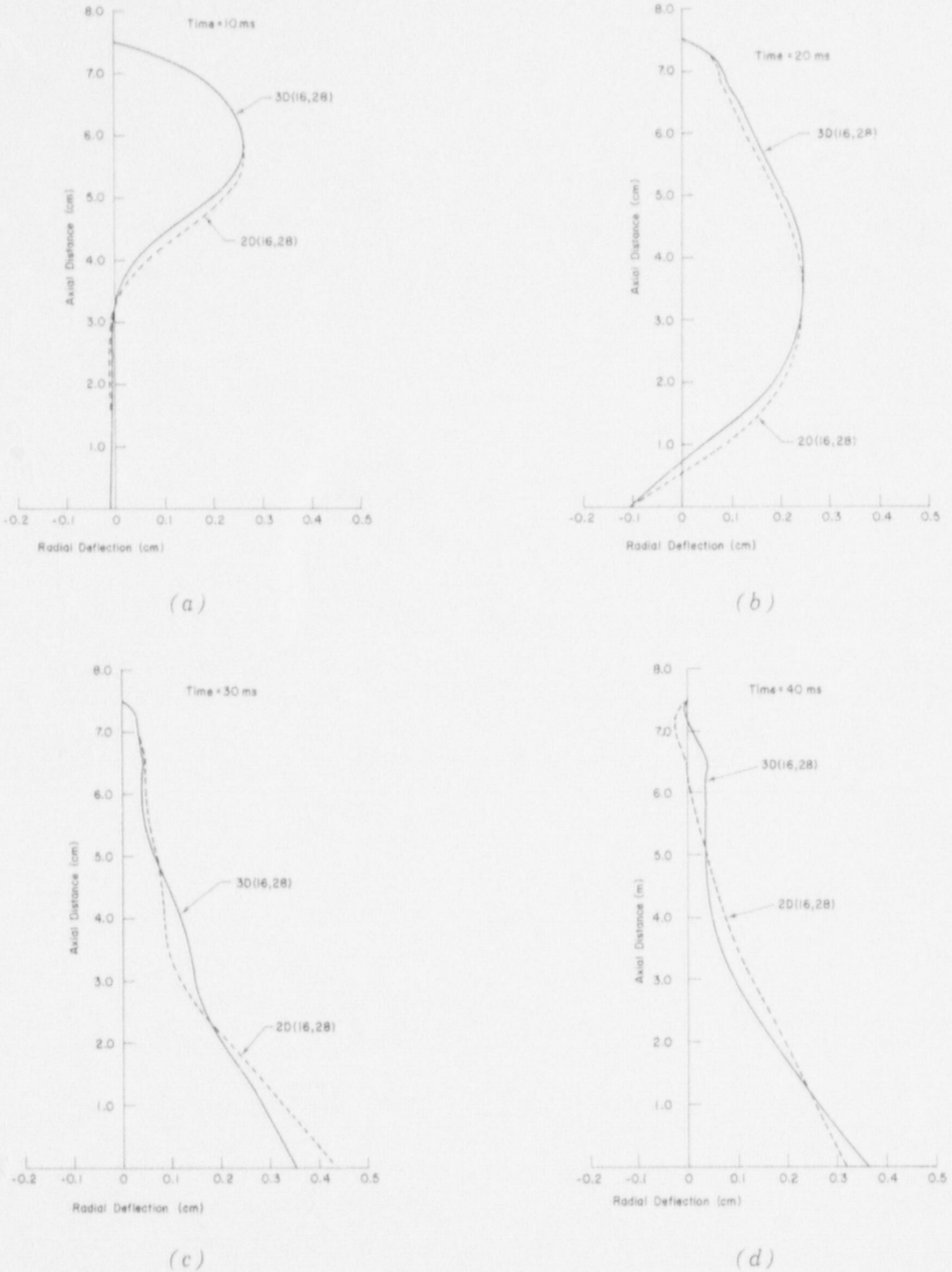

Fig. 8.

Radial deflections of the core barrel in the plane $\phi = 0°$ through the break at 10, 20, 30, and 40 ms after the pipe break. The results were calculated with two- and three-dimensional fluid descriptions and structural coupling.

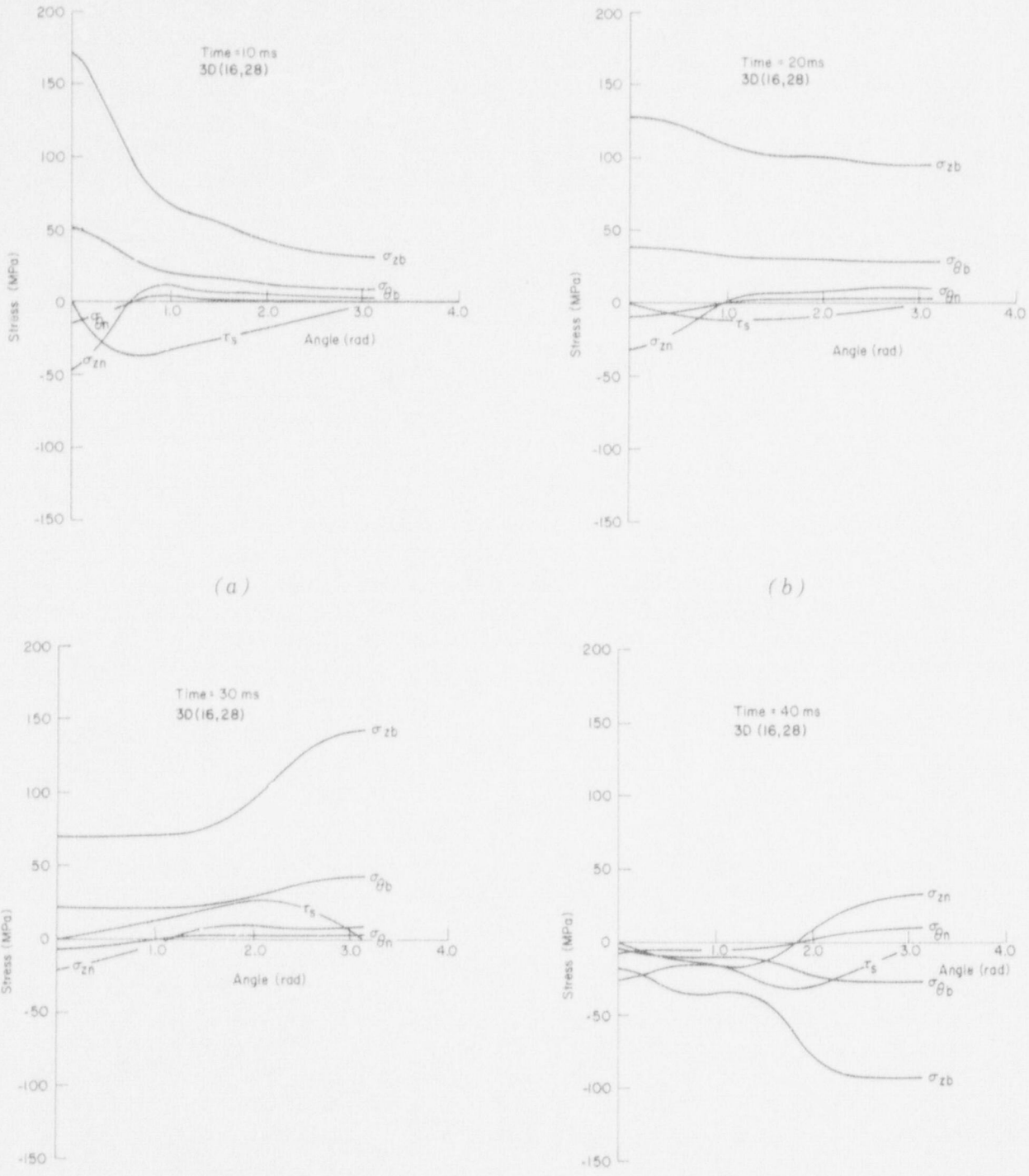

Fig. 9.

Stresses at the top of the core barrel calculated in three dimensions with fluid-structure coupling at 10, 20, 30, and 40 ms after the pipe break. The figures show the axial and circumferential bending stresses σ_{zb} and $\sigma_{\theta b}$ on the outer surface of the core barrel, the mean axial and circumferential normal stresses σ_{zn} and $\sigma_{\theta n}$, and the mean shear stress τ_s.

when the symmetric part of $\tau_{\phi x}$ is approximated as a constant τ_s. The first moment of the shear stress $\tau_{\phi x}$ that produces local twisting is so small that it was omitted from Figs. 9a-d. Figures 9a-d show the dominance of the axial bending stress at the core barrel top. Because this is the dominant stress at this location, it is chosen as the single stress to be used for comparing the two- and three-dimensional results (see Figs. 10a-d). There is good agreement to 20 ms, but from 20 to 40 ms, 25 to 40% differences occur. Comparison of stresses is a much more severe test of the adequacy of the two-dimensional description than comparison of deflections because the stresses depend on deflection derivatives.

The coupled two-dimensional calculation, which used the same time steps as the three-dimensional calculation, took only 9 min of CDC 7600 time. The 47-min reduction in computer time and the reasonably good agreement with the three-dimensional results make the two-dimensional fluid description an attractive option.

C. Effect of Mass Ring on Core Barrel Dynamics

To simulate the resistance to deformation and increased inertia of the core internal structures, it has been proposed that a massive ring (about 10^4 kg) be attached to the inside of the core barrel around its bottom boundary. Three-dimensional coupled calculations were performed to investigate the ring's effect on the core barrel dynamics. The lowest fluid cells in the core adjacent to the inside of the core barrel were made rigid obstacle cells to simulate the ring's volume. The ring significantly increases the core barrel stiffness coefficients C and D through an increase in the shell thickness h, and the increased stiffness keeps the core barrel bottom very nearly circular in cross section. The associated higher frequencies require a significant reduction in the structure time step for numerical stability. The controlling time step restriction arises from the radial acceleration equation as

$$\delta t_s \leq (\delta x)^2 \left[6\rho h (1 - \nu^2) / E h_{ring}^3 \right]^{\frac{1}{2}} .$$

which leads to $\delta t_s \leq 5.6\ \mu s$. The calculation was made with $\delta t_s = 5\ \mu s$, which is 10 times smaller than the fluid time step. The radial deflection profiles through the plane $\phi = 0°$ are compared in Figs. 11a-d. The solid curves are the three-dimensional coupled results shown in Sec. III.A that were obtained without the mass ring, whereas the dashed curves are the three-dimensional coupled results obtained with the ring. The deflection of the bottom boundary is reduced by the ring owing to the combination of increased inertia and rigidity. Deflection histories of the bottom in the plane $\phi = 0°$ are compared in Fig. 12. The ring reduces the deflection amplitude by about a factor of 2. A comparison of the axial bending stresses around the top of the core barrel is shown in Figs. 13a-d. There is no significant change in the stress magnitude at the top caused by the ring. During the first 20 ms, the axial bending stresses are nearly identical.

D. Effect of Structure Nodalization

The effect of structural noding was investigated with the two-dimensional fluid description discussed earlier for the core barrel without the mass ring. Structural noding, and particularly axial noding, is of interest because of the large axial variation in the curvature of the deformed core barrel near the top boundary. An accurate determination of the important axial bending

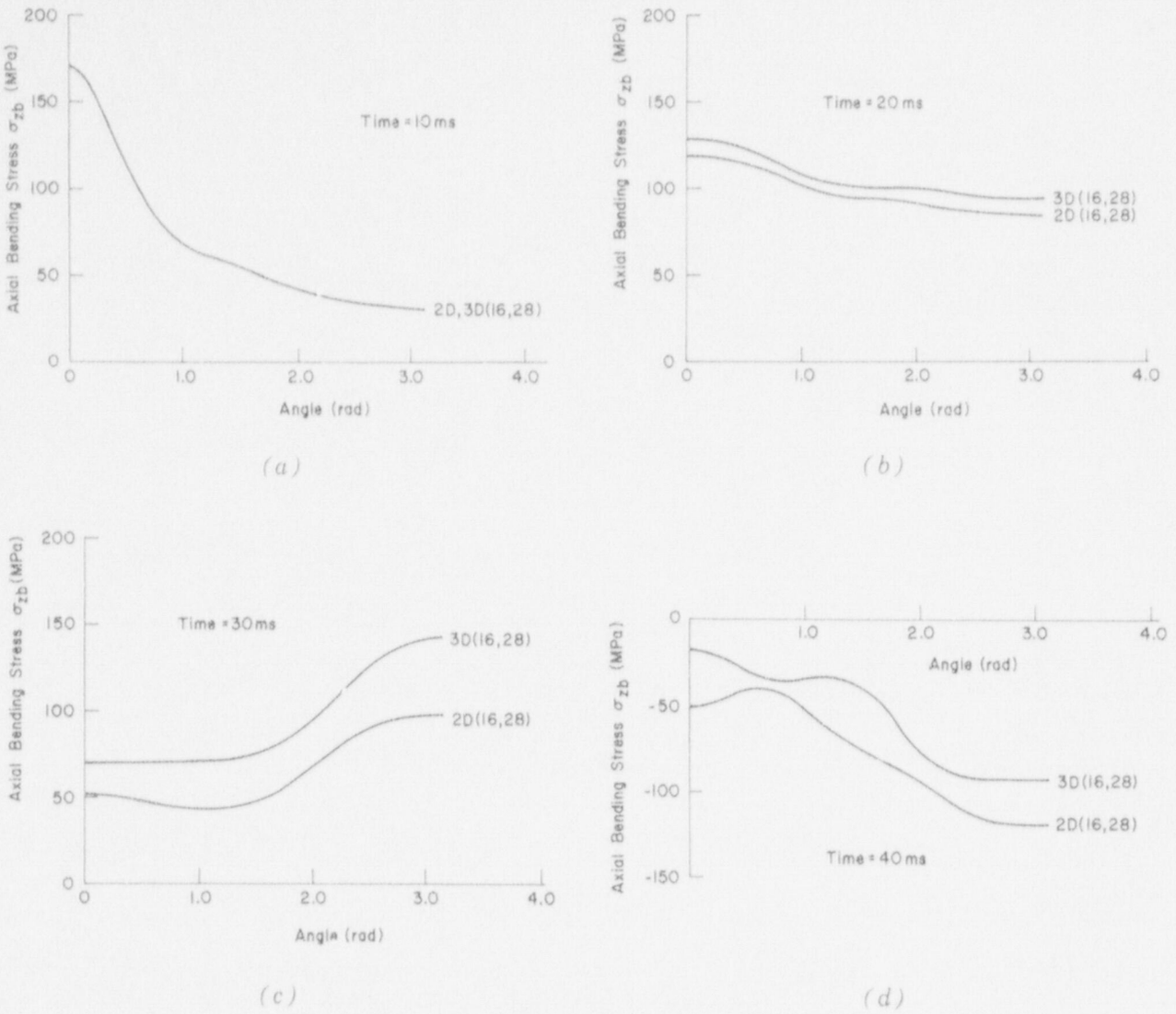

Fig. 10.

Axial bending stresses at the top, built-in boundary of the core barrel calculated with two- and three-dimensional fluid descriptions and structural coupling at 10, 20, 30, and 40 ms after the pipe break.

stress at the top depends directly on the local curvature. The effect of the uniform circumferential noding is investigated first to ensure sufficient resolution in this direction before considering the axial noding. Circumferential spacings at 12°, 6°, and 3° intervals are considered. The 12° spacing is the standard noding used previously. Results for the 12° noding, labeled A(16,28), are the same as the two-dimensional results presented earlier for the two- and three-dimensional fluid simulation comparison. Results for the 6° noding are labeled B(31,28) and for the 3° noding, C(61,28). For these calculations, the axial noding is the standard 28-node arrangement described earlier. The radial deflection profiles in the plane $\phi = 0°$ are compared in Figs. 14a-d and 15a-d. The calculated axial bending stresses are compared in Figs. 16a-d for the three cases. Results show that the 6° interval provides adequate circumferential resolution because curves B(31,28) and C(61,28) are very nearly coincident.

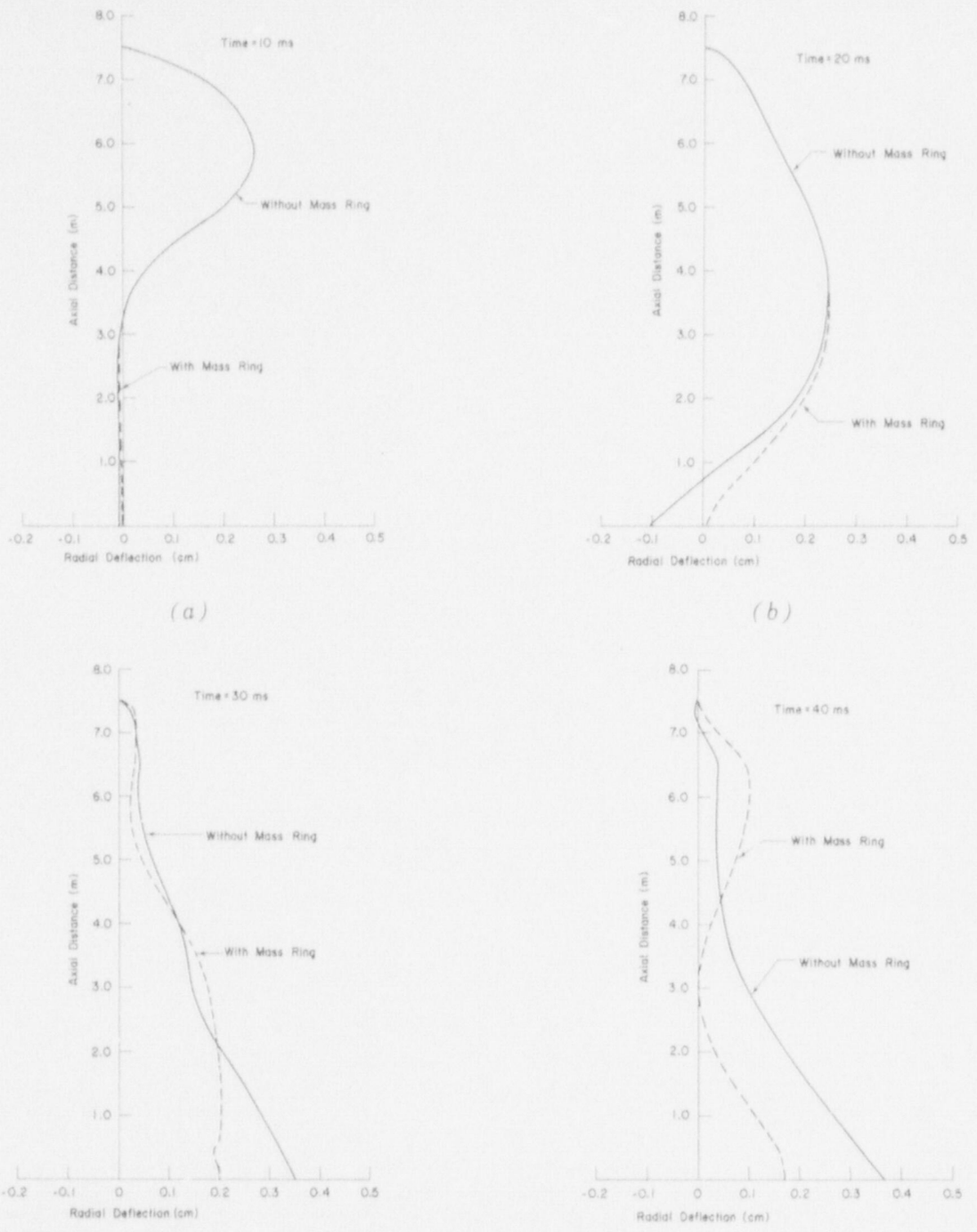

Fig. 11.
Radial deflections of the core barrel in the plane $\phi = 0°$ through the break at 10, 20, 30, and 40 ms after the pipe break. The results were calculated in three dimensions with and without the bottom ring.

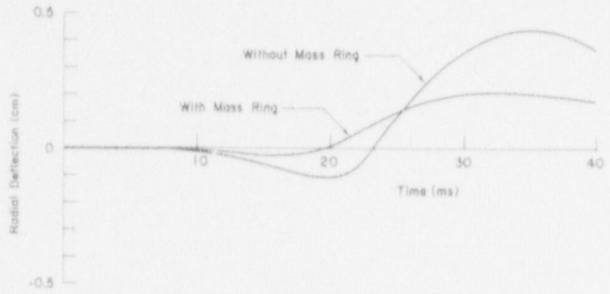

Fig. 12.
Radial deflection of the core barrel bottom directly below the break calculated in three dimensions with and without the bottom ring.

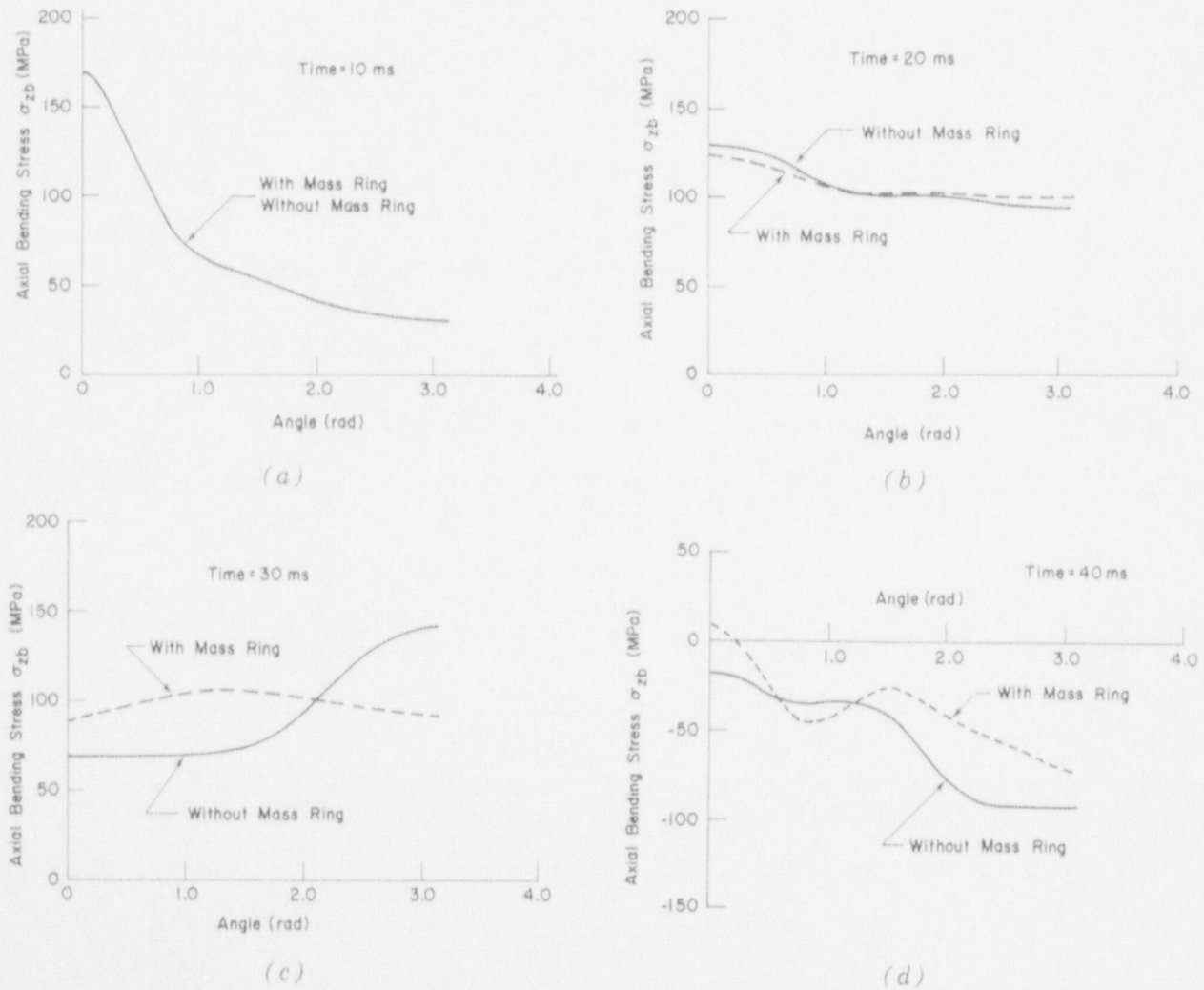

Fig. 13.
Axial bending stresses at the top, built-in boundary of the core barrel calculated in three dimensions with and without the bottom ring at 10, 20, 30, and 40 ms after the pipe break.

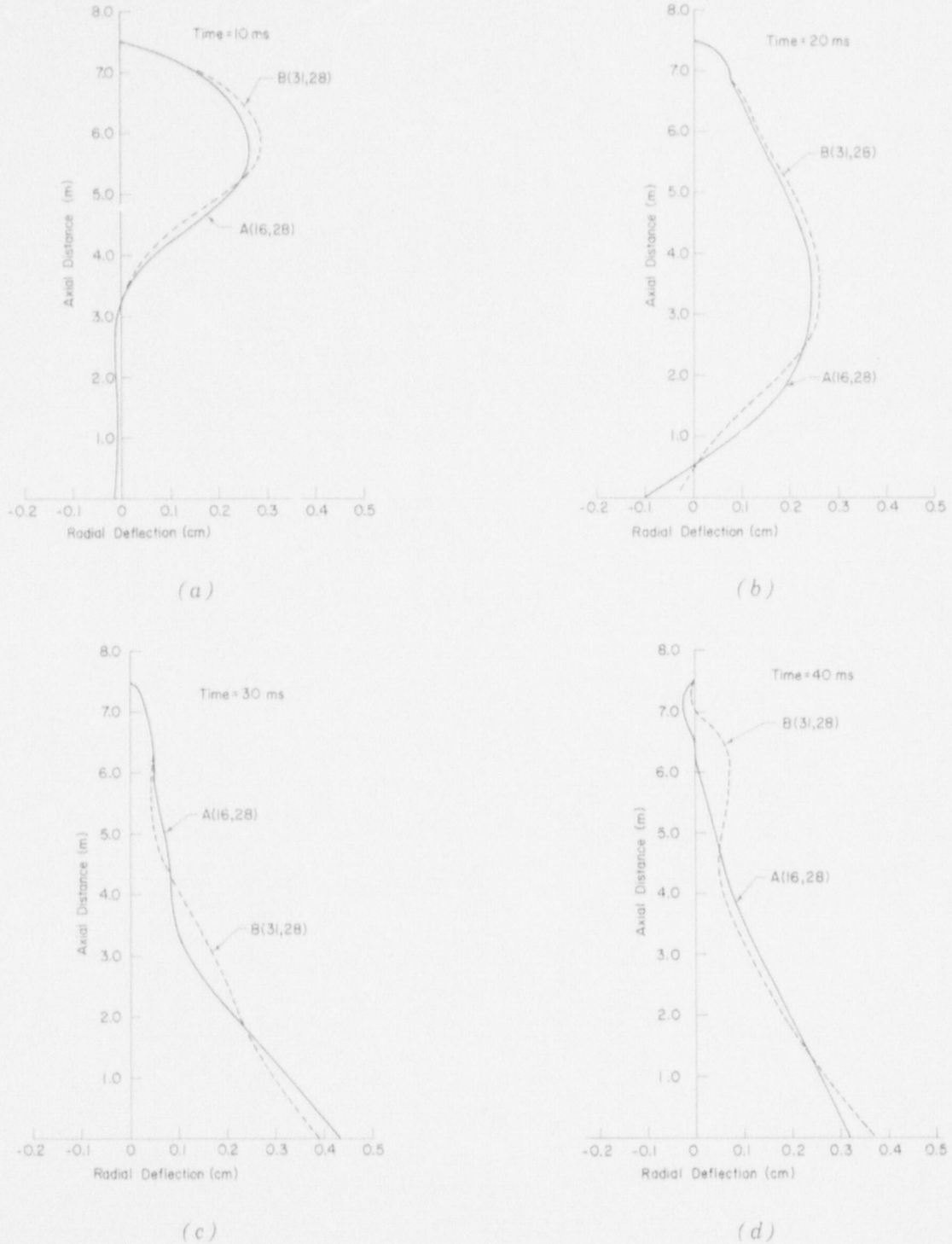

Fig. 14.
Radial deflections of the core barrel in the plane $\phi = 0°$ through the break at 10, 20, 30, and 40 ms after the pipe break. The results were calculated with the two-dimensional fluid description for 12° (case A) and 6° (case B) circumferential noding.

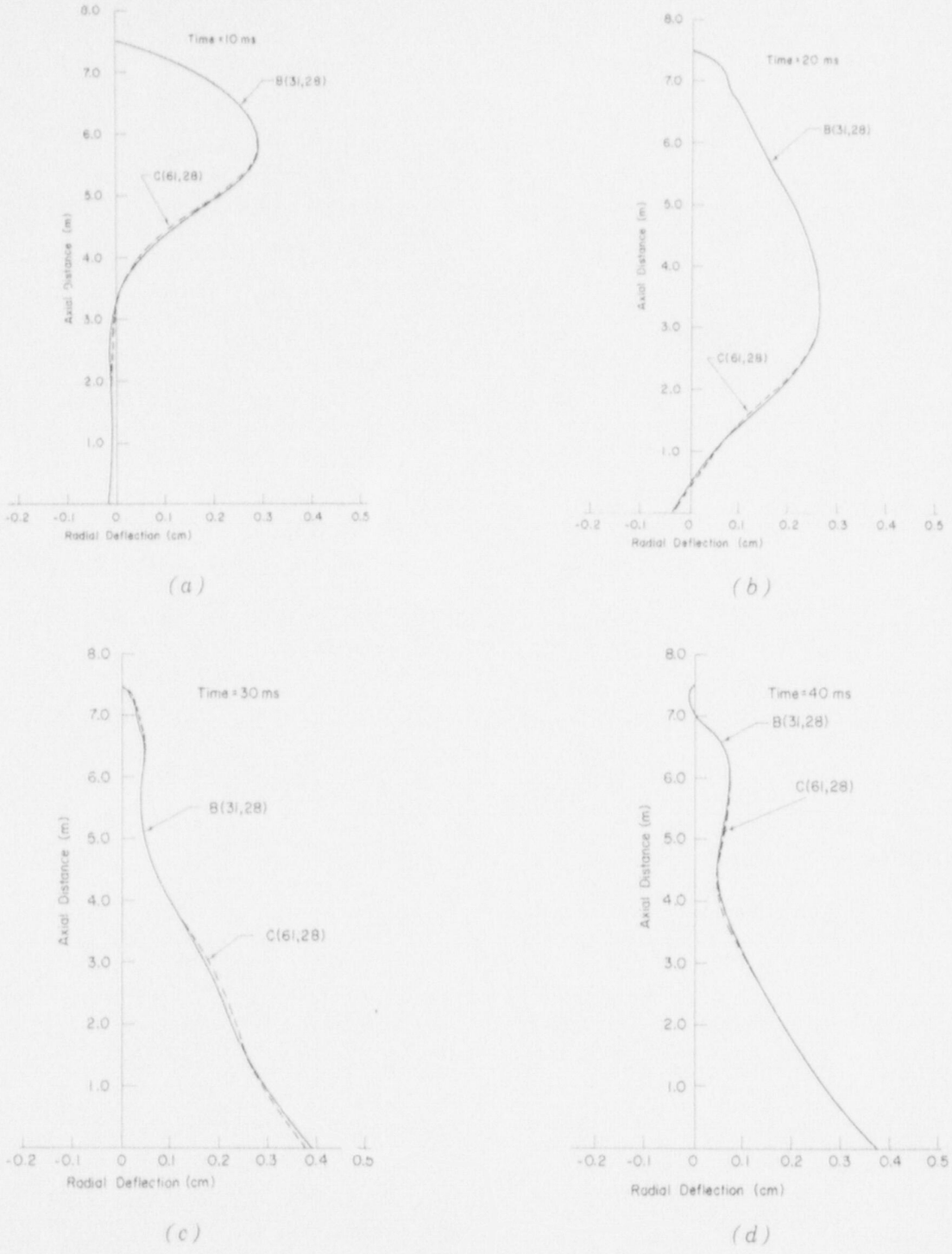

Fig. 15.
Radial deflections of the core barrel in the plane $\theta = 0°$ through the break at 10, 20, 30, and 40 ms after the pipe break. The results were calculated with the two-dimensional fluid description for 6° (case B) and 3° (case C) circumferential noding.

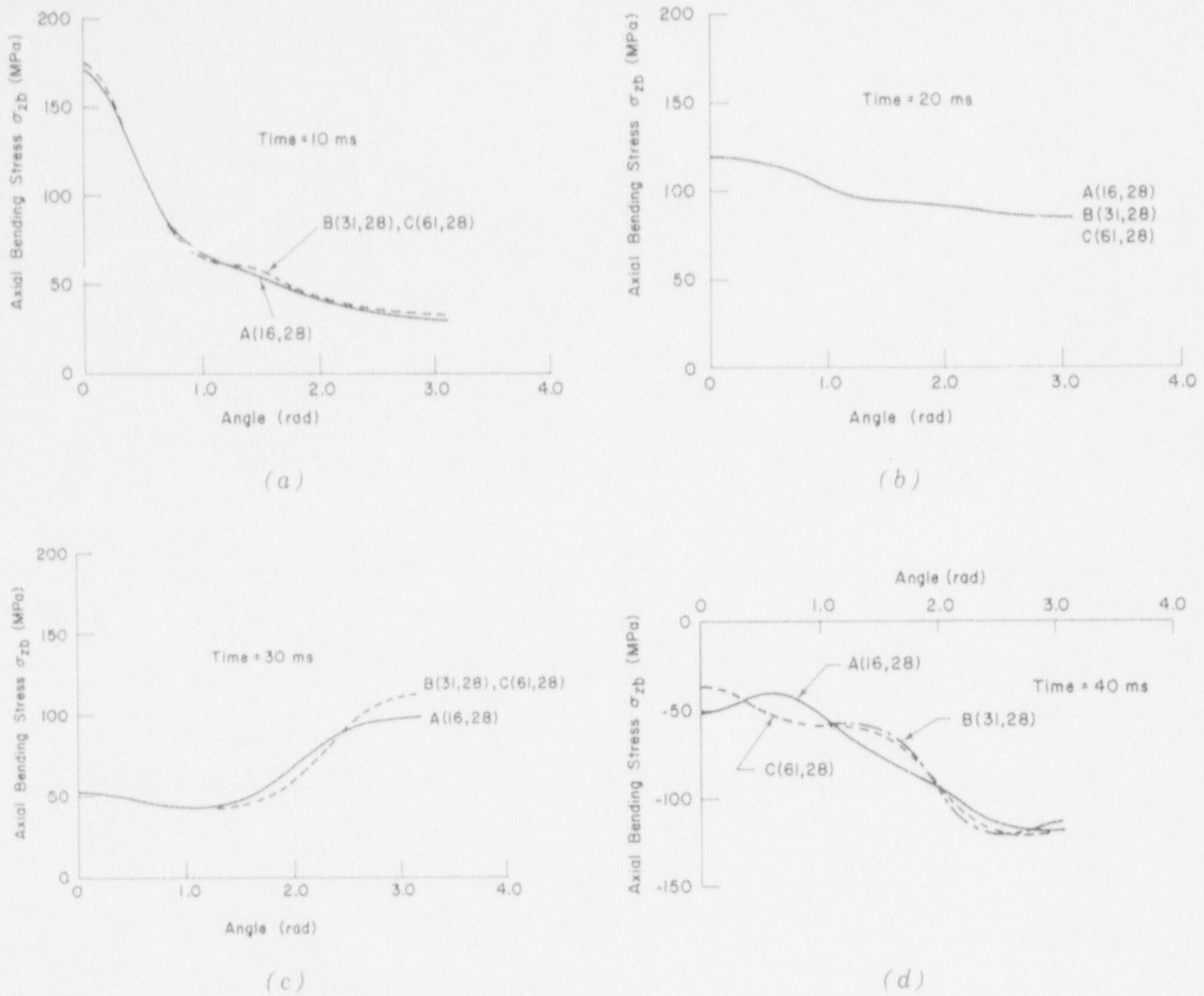

Fig. 16.
Axial bending stresses at the top, built-in boundary of the core barrel calculated with the two-dimensional fluid description for 12° (case A), 6° (case B), and 3° (case C) circumferential nodings at 10, 20, 30, and 40 ms after the pipe break.

The effects of axial noding were investigated by successively finer zoning of the region near the core barrel top and by using the 6° spacing for circumferential noding. Table I lists the axial coordinates of the standard B(31,28) and two finer nodalizations D(31,32) and E(31,38). The calculated radial deflections in the plane $\phi = 0°$ are compared in Figs. 17a-d for cases B and D. Radial deflections for case E are coincident with those for case D. Axial bending stresses at the core barrel top are compared in Figs. 18a-d. Again, cases D and E produce coincident results. The axial bending stress is about 20% greater for cases D and E than for case B. The spacing interval of 0.072 m near the top boundary provides sufficient axial resolution for an accurate determination of the bending stress. For an axisymmetric deformation of the core barrel, Dienes et al.[5] have shown that the axial bending stress varies most rapidly near the core barrel top over a distance $\Delta x = \pi/\beta$, where $\beta^4 = 3(1-\nu^2)/a^2h^2$. For the present geometry, this distance is $\Delta x = 0.426$ m, which is resolved by 3, 5, and 8 nodes for cases B, D, and E, respectively.

TABLE I

LOCATION OF AXIAL NODES RELATIVE TO THE CORE BARREL TOP BOUNDARY

Node	B(31,28)	D(31,32)	E(31,38)
1	0.	0.	0.
2	0.144	0.072	0.036
3	0.432	0.144	0.072
4	0.720	0.240	0.120
5	1.008	0.360	0.180
6	1.296	0.504	0.252
7	1.584	0.672	0.336
8	1.872	0.864	0.432
9	2.160	1.080	0.540
10	2.448	1.320	0.660
11	2.736	1.584	0.792
12	3.024	1.872	0.936
13	3.312	2.160	1.092
14	3.600	2.448	1.260
15	3.888	2.736	1.440
16	4.176	3.024	1.632
17	4.464	3.312	1.836
18	4.752	3.600	2.052
19	5.040	3.888	2.280
20	5.328	4.176	2.520
21	5.616	4.464	2.772
22	5.904	4.752	3.036
23	6.192	5.040	3.312
24	6.480	5.328	3.600
25	6.768	5.616	3.888
26	7.056	5.904	4.176
27	7.344	6.192	4.464
28	7.488	6.480	4.752
29		6.768	5.040
30		7.056	5.328
31		7.344	5.616
32		7.488	5.904
33			6.192
34			6.480
35			6.768
36			7.056
37			7.344
38			7.488

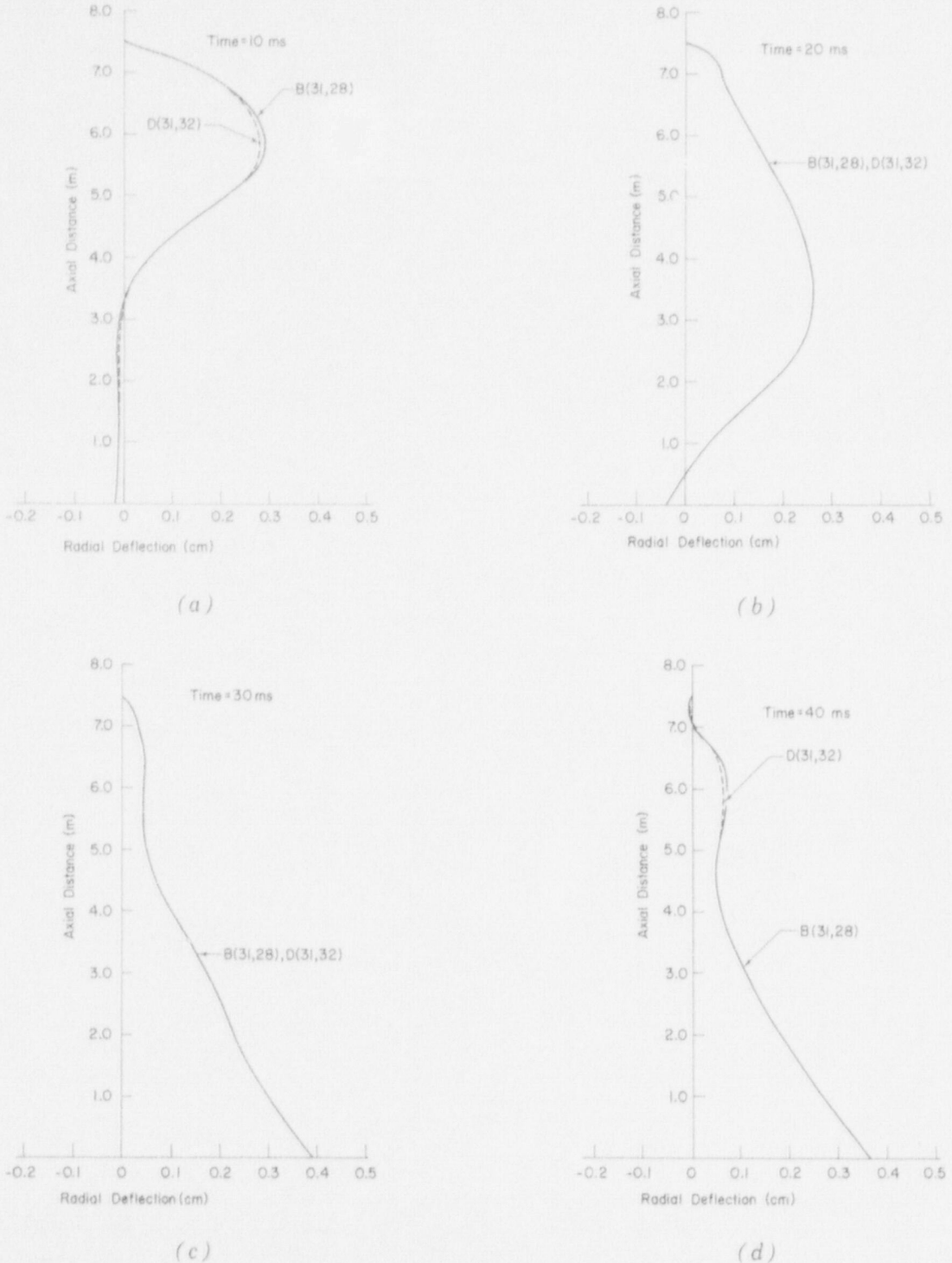

Fig. 17.
Radial deflections of the core barrel in the plane $\phi = 0°$ through the break at 10, 20, 30, and 40 ms after the pipe break. The results were calculated with the two-dimensional fluid description for the axial nodings given in Table I.

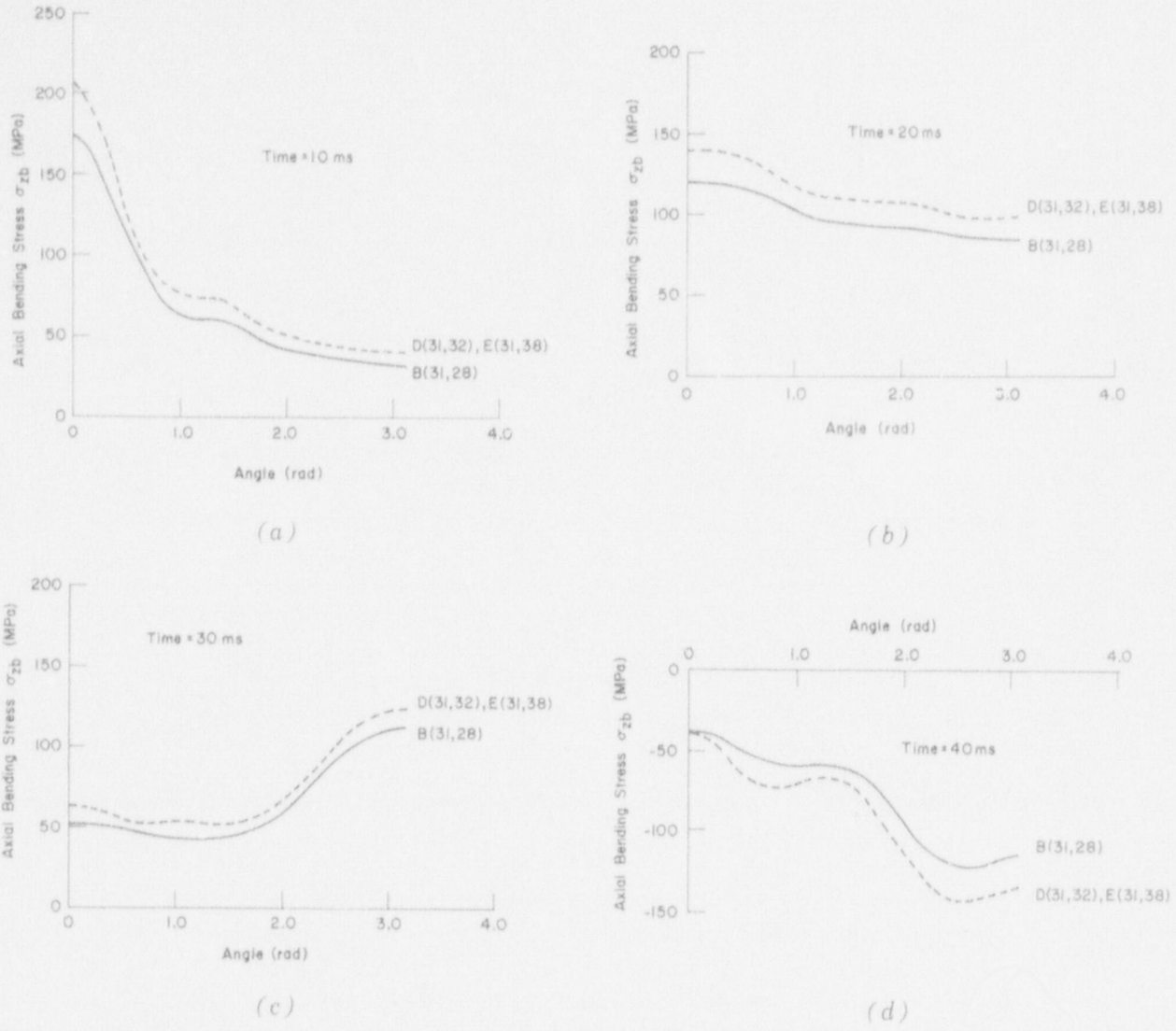

Fig. 18.
Axial bending stresses at the top, built-in boundary of the core barrel calculated with the two-dimensional fluid description for the axial nodings given in Table I at 10, 20, 30, and 40 ms after the pipe break.

IV. CONCLUSIONS

Results of the three-dimensional calculations with K-FIX for an HDR reactor vessel blowdown with and without fluid-structure coupling have shown the importance of coupling on the core barrel dynamics. The coupled results show a lower frequency and a lower amplitude motion than the uncoupled results, with the consequence of generally lower induced stresses.

Although the fluid dynamics is truly three dimensional, the utility of a two-dimensional description has been demonstrated. A two-dimensional calculation of the fluid motion in the downcomer annulus together with a simple model for the time variation of pressure in the lower plenum and core region produces good results for the core barrel dynamics. The calculated

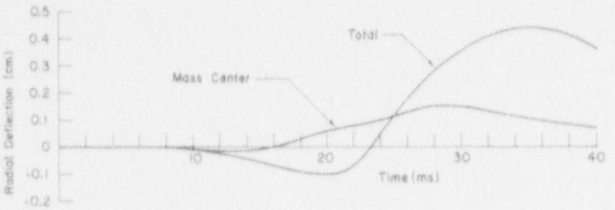

Fig. 19.
Total radial deflection of the core barrel bottom directly below the break compared with the corresponding center of mass displacement.

stresses are quite accurate to 20 ms and show differences of about 30% by 40 ms. The two-dimensional fluid calculation coupled with the solution of the three-dimensional shell equations requires about 9 min of CDC 7600 time, whereas the three-dimensional calculation requires about 55 min.

The addition of a massive ring attached to the core barrel bottom to simulate the stiffness and inertia of internal structure reduces the deflection amplitude at the bottom, but the effect is primarily local. Stresses at the top, built-in boundary of the core barrel, which is where maximum stress often occurs, are not altered significantly.

Sensitivity of the calculated results to the axial and circumferential noding of the core barrel was investigated. Our tests show that relatively fine axial spacing is required near the top boundary for an accurate stress calculation. An axial spacing that gave good results began with an interval of about 1% of the core barrel length, increased linearly to about 4% over the top one-fifth of the length, and thereafter remained constant. The circumferential spacing was less critical. A 6° interval provided adequate resolution.

The deflection of the core barrel in an axial plane reflects the combination of deflection of the mass center and distortion. The relative importance of these contributing elements is shown in Fig. 19, in which the total radial deflection of the core barrel bottom boundary in the plane $\phi = 0°$ is compared to the corresponding radial deflection of the mass center. The distortional contribution clearly dominates the total deflection.

REFERENCES

1. R. Krieg, E. G. Schlechtendahl, and K.-H. Scholl, "Design of the HDR Experimental Program on Blowdown Loading and Dynamic Response of PWR-Vessel Internals," Nucl. Eng. Des. **43**, 419 (1977).

2. R. Krieg, E. G. Schlechtendahl, K.-H. Scholl, and U. Schumann, "Full-Scale HDR Blowdown Experiments as a Tool for Investigating Dynamic Fluid-Structural Coupling," Proc. 4th Int. Conf. Structural Mechanics in Reactor Technology, San Francisco, California, August 15-19, 1977, paper B5/1 (1978).

3. E. G. Schlechtendahl, R. Krieg, U. Schumann, and C. W Hirt, "Analyse der Fluidstrukturdynamischen Wechselwirkung von Reaktordruckbehaltereinbauten beim Blowdown," Kernforschungszentrum Karlsruhe Projekt Nukleare Sicherheit report KfK 2570 (1977).

4. W. C. Rivard and M. D. Torrey, "K-FIX: A Computer Program for Transient, Two-Dimensional, Two-Fluid Flow," Los Alamos Scientific Laboratory report LA-NUREG-6623 (April 1977).

5. J. K. Dienes, C. W. Hirt, and L. R. Stein, "Computer Simulation of the Hydroelastic Response of a Pressurized Water Reactor to a Sudden Depressurization," Los Alamos Scientific Laboratory report LA-NUREG-6772-MS (April 1977).

6. F. H. Harlow and A. A. Amsden, "A Numerical Fluid Dynamics Calculation Method for All Flow Speeds," J. Comp. Phys. 8, 197-213 (1971).

7. S. Timoshenko, **Theory of Plates and Shells** (McGraw-Hill Book Co., New York, 1940).

8. W. C. Rivard and M. D. Torrey, "Nuclear Reactor Safety Quarterly Progress Report, April 1—June 30, 1977," Los Alamos Scientific Laboratory report LA-NUREG-6934-PR, p. 19 (August 1977).

☆ U.S. GOVERNMENT PRINTING OFFICE 1978—677-013/168

Available from
US Nuclear Regulatory Commission
Washington, DC 20555

Available from
National Technical Information Service
Springfield, VA 22161

Microfiche	$ 3.00	126-150	7.25	251-275	10.75	376-400	13.00	501-525	15.25
001-025	4.00	151-175	8.00	276-300	11.00	401-425	13.25	526-550	15.50
026-050	4.50	176-200	9.00	301-325	11.75	426-450	14.00	551-575	16.25
051-075	5.25	201-225	9.25	326-350	12.00	451-475	14.50	576-600	16.50
076-100	6.00	226-250	9.50	351-375	12.50	476-500	15.00	601-up	--1
101-125	6.50								

1. Add $2.50 for each additional 100-page increment from 601 pages up.